LASER & PHOTONICS REVIEWS

www.lpr-journal.org

Multilayer Polymer Shell Perfluoropentane Nanodroplets for Multimodal Ultrasound, Magnetic Resonance, and Optoacoustic Imaging

Elizaveta A. Maksimova, Daniil Nozdriukhin, Sandeep Kumar Kalva, Shuxin Lyu, Berkan Lafci, Mark-Aurel Augath, Polina G. Rudakovskaya, Alexander A. Solovev, Yongfeng Mei, Xosé Luís Deán-Ben, Daniel Razansky,* and Dmitry A. Gorin**

Multimodal imaging increases the value of stand-alone modalities by enabling simultaneous multiparametric characterization of biological tissues in vivo. Particularly, optoacoustic (OA) tomography has enabled bringing optical imaging advantages to previously unattainable depths and is currently being hybridized with other imaging technologies for enhanced performance. The full potential of these multimodal imaging approaches can only be achieved with dedicated contrast agents ensuring simultaneous measurements and accurate co-registration of the information provided. Herein, perfluoropentane-filled nanodroplets are modified, providing excellent contrast in ultrasound imaging, by introducing shell-embedded additives offering strong contrast in magnetic resonance and OA imaging. Magnetite nanoparticles and indocyanine green (ICG) dye are simultaneously deposited as a multilayer shell on the droplets with the layer-by-layer method. This results in sufficiently high amounts of magnetite (0.54 ± 0.08 mg mL^{-1}) and ICG (0.30 ± 0.08 mg mL^{-1}) for efficient magnetic resonance and OA detection, respectively. The high sensitivity achieved with the developed trimodal nanodroplets is first demonstrated in phantom experiments, after which their potential toxic effects, biodistribution, and clearance are examined in vitro and in vivo. Taken together, the obtained results indicate that the developed multilayer polymer shell nanodroplets are efficient hybrid contrast agents for multimodal biomedical imaging applications.

1. Introduction

Biomedical imaging techniques are essential tools in preclinical research as well as for patient diagnosis and monitoring in the clinical setting. Ultrasound (US) imaging is, along with planar X–ray, the most widely-used clinical imaging modality.[1] It is non-invasive, radiation-free, relatively cheap, and can render high-resolution images in real time, thus enabling bedside examination of human body parts in a safe hand-held manner. Physicians are well-trained for the interpretation of US images of different regions according to well-established guidelines.[2] However, the acquired images and hence the results of a scan greatly depend on the operator.[3] Moreover, attenuation and distortion of US waves prevent access to certain parts of the human body such as the brain.[4] Whole-body imaging modalities enable anatomical visualization of any region of the human body. Magnetic resonance imaging (MRI) is arguably the most powerful anatomical imaging approach as it overcomes the limitations of X-ray

E. A. Maksimova, P. G. Rudakovskaya, D. A. Gorin
Center for Photonics Science and Engineering
Skolkovo Institute of Science and Technology
Bolshoy Boulevard 30, Building 1, Moscow 121205, Russia
E-mail: d.gorin@skoltech.ru

D. Nozdriukhin, S. K. Kalva, S. Lyu, B. Lafci, X. L. Deán-Ben, D. Razansky
Institute for Biomedical Engineering and Institute of Pharmacology and Toxicology, Faculty of Medicine
University of Zürich
Winterthurerstrasse 190, Zurich 8057, Switzerland
E-mail: xl.deanben@pharma.uzh.ch; daniel.razansky@pharma.uzh.ch

D. Nozdriukhin, S. K. Kalva, S. Lyu, B. Lafci, M.-A. Augath, X. L. Deán-Ben, D. Razansky
Institute for Biomedical Engineering
Department of Information Technology and Electrical Engineering
ETH Zürich, Rämistrasse 101, Zurich 8093, Switzerland

S. Lyu
Department of Medical Imaging
Shanxi Medical University
Taiyuan 030001, China

A. A. Solovev, Y. Mei
Department of Materials Science
Fudan University
Shanghai 200433, China

The ORCID identification number(s) for the author(s) of this article can be found under https://doi.org/10.1002/lpor.202300137

DOI: 10.1002/lpor.202300137

computed tomography (CT) in terms of lack of soft-tissue contrast and use of ionizing radiation. MRI can resolve morphological changes in biological tissues and organs with high resolution, but is afflicted by high equipment and maintenance costs, low molecular specificity, and low sensitivity to extrinsically-administered contrast agents.[5] By synergistically combining interrogation of biological tissues with light and US detection, optoacoustic (OA, photoacoustic) imaging emerged as a new optical imaging modality complementing the contrast limitations of US imaging and MRI by providing otherwise-unavailable functional and molecular information from deep-located biological tissues with high-resolution.[6–9] Recently, OA imaging has also been used in initial clinical trials supported by the powerful capabilities demonstrated in multiple preclinical studies in the last decade.[10–12] Being based on US detection, OA imaging has been combined with US imaging to facilitate its clinical acceptance.[13–16] Also, the feasibility of simultaneous OA-MRI imaging has been demonstrated with a dedicated hybrid system,[17,18] which enabled unprecedented capabilities in neuroscience and is also poised to impact other biological fields.[19] Multimodal US-MRI-OA imaging can then emerge as a new approach providing never-seen-before multiparametric anatomical, functional and molecular contrast at different spatial and temporal scales. Co-registration of the information provided by these modalities is however hampered by the fundamentally different contrast mechanisms, also resulting in sensitivity differences. Dedicated contrast agents providing sufficient sensitivity in all modalities to enable simultaneous dynamic measurements are then essential to fully exploit the potential capabilities of this multimodal approach.

Multiple types of contrast agents for MRI, US and OA imaging have been developed, thoroughly studied, and/or marketed. These provide anatomical and functional information not available from the endogenous contrast of tissue components. Commonly used agents are gas-filled microbubbles in US imaging,[20,21] paramagnetic compounds and gadolinium-coordination complexes in MRI,[22,23] and organic dyes and nanoparticles in OA imaging.[24–26] Yet, no significant efforts have been directed to the development of multimodal agents providing sufficient contrast in all three modalities, arguably due to the lack of multi-modal imaging systems hybridizing OA with US or MRI. Multimodal contrast agents have gained enormous attention as they enable combining synergistic functions to provide a comprehensive evaluation of normal and pathological tissues.[27–29] Multimodal strategies based on complementary imaging techniques are capable of providing fast and accurate diagnosis. The use of multimodal contrast agents can reduce costs and decrease the invasiveness of examinations by limiting the administered dose. Additionally, multifunctional contrast agents can assist blood-brain barrier crossing[30,31] and intraoperative imaging,[32] as well as enable advanced theranostic approaches if combined with therapeutic substances.

US contrast agents based on low-boiling-point liquid nanodroplets have been developed as an alternative to conventional microbubbles. These have become promising platforms for the incorporation of molecular imaging additives into shells. Usually, a liquid core of perfluorocarbons (PFCs), e.g. perfluoro-butane (PFB), -pentane (PFP), or -hexane (PFH) leads to improved droplet stability owing to their insolubility in water and other liquids.[33] Apart from providing blood-pool contrast, submicron-sized PFP-filled droplets can extravasate the tumor vascular system, after which they can be evaporated by laser or US pulses to provide tumor-specific contrast. A drastic expansion in bubble size of up to 30 μm has been observed.[34] These gas-filled bubbles provide higher echogenicity than in their native liquid-core state and produce higher US contrast owing to the nonlinear compression–expansion effects of the gas core.[35,36] Optical activation of the droplets can be achieved with pulsed-laser irradiation absorbed by chromophores incorporated in the droplet shell or dissolved in the PFC core.[37] For example, near-infrared (NIR) absorbing substances such as clinically-approved indocyanine green (ICG),[38] Epolight,[36] and polypyrrole nanoparticles[39] have been used for this purpose. The absorbed energy is transferred into heat, which facilitates core vaporization and further expansion. Liquid phase vaporization can alternatively be achieved with the application of cyclic pressure waves of US. Discovered in 1995, this phenomenon is now termed acoustic droplet vaporization.[40] Acoustic droplet vaporization is preferred to laser-triggered vaporization as US transducers are more accessible than lasers and no additional droplet-shell components are needed.[40] Recently, contrast agents based on PFB have been approved for clinical use in several countries.[41] However, PFB is a gas at normal conditions (boiling point of -1.7°C), which hampers its use. PFP has a lower boiling point than other perfluorocarbons, which is an important advantage as it facilitates conversion from liquid to gas phases under ultrasound or laser excitation.

In a few studies, nanodroplets incorporating magnetite (Fe_3O_4) nanoparticles and ICG or other dyes have been suggested. Niu et al. developed novel PFP-based poly(lactic-*co*-glycolic acid) (PLGA)-encased nanodroplets loaded with Fe_3O_4 nanoparticles and ICG as nanotheranostic agents for photothermal tumor ablation.[42] The authors report that both Fe_3O_4 and ICG are capable of converting absorbed NIR light to heat, facilitating the evaporation of PFP to enhanced thermal ablation in tumor areas. They report these dual polymeric droplets could be used as effective theranostic agents, yet, this contrasting ability was not shown for any of the additives. Thus, the influence of different modalities on each other remained unclear. Wang et al. showed that simultaneous incorporation of Fe_3O_4 and IR780 iodide in PLGA-coated PFP droplets enables trimodal (US-MRI-OA) imaging and can assist doxorubicin release with great potential in cancer theranostics.[43] Lemaster et al. proposed a PLGA-based iron oxide nanobubbles labelled with 1,1′-dioctadecyl-3,3,3′,3′-tetramethylindotricarbocyanine iodide as a trimodal (US-MRI-OA) contrast agent for stem cells imaging. In this study, both dye and nanoparticles were incorporated by direct dissolution in the hydrophobic core.[44]

In this work, we suggest using the layer-by-layer (LbL) approach for the development of nanodroplets providing trimodal contrast. First described in 1991 by Decher et al., this method produces multilayer ultrathin organic films by sequential deposition of aqueous solutions of oppositely charged polyelectrolytes on solid substrates.[45] Since then, various polyelectrolyte capsules made from different compounds have been reported.[46–49] LbL deposition is more reproducible than alternative methods and offers high loading efficiency. Conventionally, charged substances have been deposited on a solid template, followed by

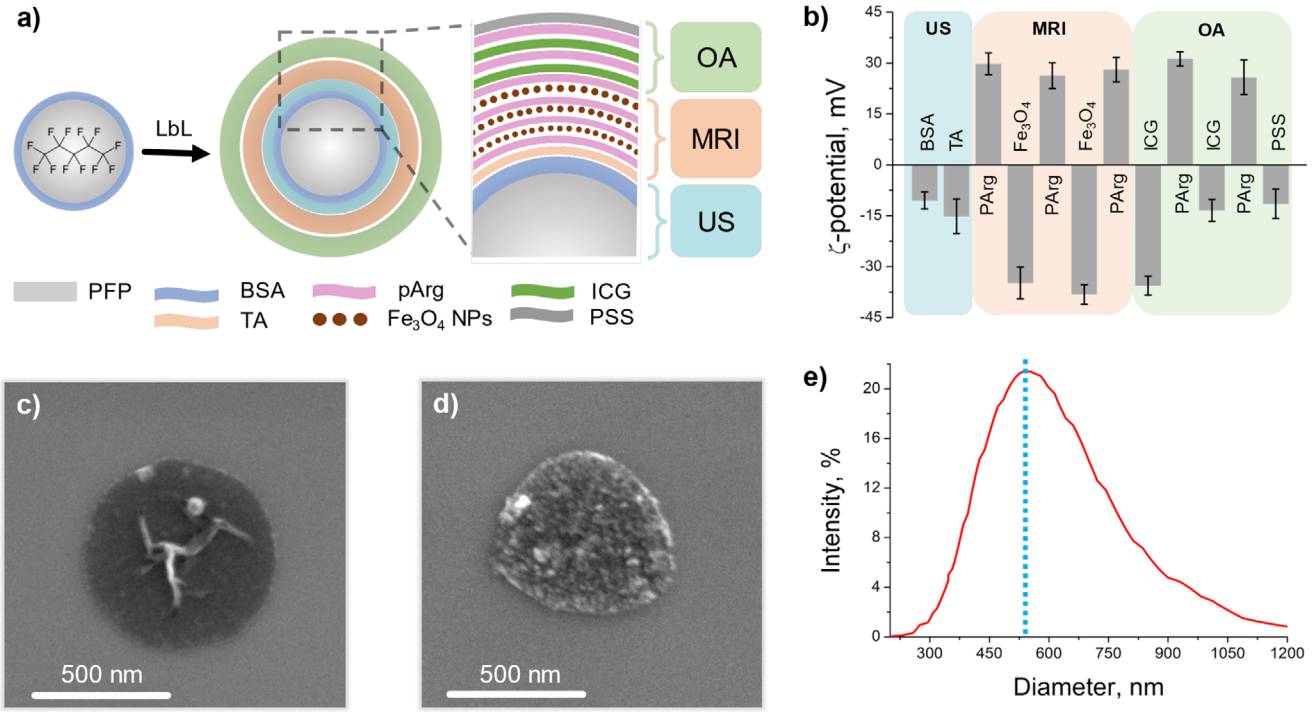

Figure 1. a) Schematic representation of the preparation of nanodroplets and functionalization with magnetite and ICG by the LbL approach (PFP = perfluoropentane, Fe_3O_4 NPs = magnetite nanoparticles, BSA = bovine serum albumin, TA = tannic acid, PArg = poly-L-arginine, ICG = indocyanine green, PSS = poly(styrene sulfonate). b) Dependence of the ζ-potential on the deposition of oppositely charged layers. c) SEM image of a load-free PFP–BSA nanodroplet. d) SEM image of a PFP nanodroplet loaded with ICG and magnetite. e) Size distribution of the resulting nanodroplets measured with dynamic light scattering (DLS).

subsequent dissolution to form a capsule.[50,51] The LbL approach has rarely been used to coat liquid or gaseous cores. Examples include the incorporation of magnetite and Cy3 on the surface of polyvinyl alcohol-coated air-filled microbubbles via alternating layers of polycations[52] and deposition of poly(allylamine hydrochloride)/poly(styrene sulfonate) onto Tween:Span air microbubbles.[53] Also, the LbL approach has been used to make drug delivery systems based on hydrophobic liquid cores initially stabilized with surfactants.[54] However, to the best of our knowledge, it has never been used with PFP. We report on a combination of submicron PFP droplets with ICG and magnetite nanoparticles incorporated into their shells. Such a structure is shown to produce high signals in all three modalities (US, MRI and OA) in both phantom experiments and in vivo.

2. Results and discussion

2.1. Nanodroplet Characterization

The sequence of layers for magnetite and ICG deposition on the PFP nanodroplets is schematically depicted in **Figure 1**a. This indicates which layers contribute to generating contrast in each modality. Initially, BSA-stabilized PFP nanodroplets were synthesized on ice to prevent rapid evaporation of PFP, with a boiling point of 29 °C. However, once entrapped in a protein shell, Laplace pressure drastically increases the boiling point up to 47 °C (Equation S1, Supporting Information). This enables layer deposition on the nanodroplets at ambient temperature.[55] Overall, three Fe_3O_4 bilayers and two ICG bilayers were deposited on the Fe_3O_4/ICG nDs as described in the methods section. The BSA-stabilized PFP nanodroplets were coated with a tannic acid layer, which conjugates through hydrophobic interactions and hydrogen bond formation.[56] The LbL method was chosen because of the following advantages: 1) on average, it offers higher loading efficiencies than direct loading, and 2) it does not require functional substances to be highly hydrophobic and soluble in PFP as it is based on either electrostatic interactions or hydrogen bond formation between neighboring layers.[46]

Successful embedding of Fe_3O_4 nanoparticles and ICG inside the nanodroplet shell was indirectly shown by ζ-potential measurements (Figure 1b). Each of these additives has a strong negative charge provided by citrate anions for magnetite and sulfonate groups for ICG. Thereby, they could be electrostatically deposited on the positively charged layer of PArg on the droplet surface.

Figure 1c,d show SEM images of the shells of PFP nanodroplets. Note that sample preparation requires drying of the droplets and imaging is done under high vacuum conditions. Therefore, PFP evaporates easily and either diffuses away or breaks through the shells, leaving them cracked open. Yet, surface morphological differences between the load-free (Figure 1c) and loaded (Figure 1d) nanodroplets could be observed. The shells of magnetite-containing nanodroplets are clearly grained, whereas those of uncoated droplets seem smooth. The SEM microphotographs also show that the droplet size is in good agreement with that measured by DLS: 500 ± 200 nm by DLS (Figure 1e) and 600 ± 300 nm by SEM. It has been shown that the

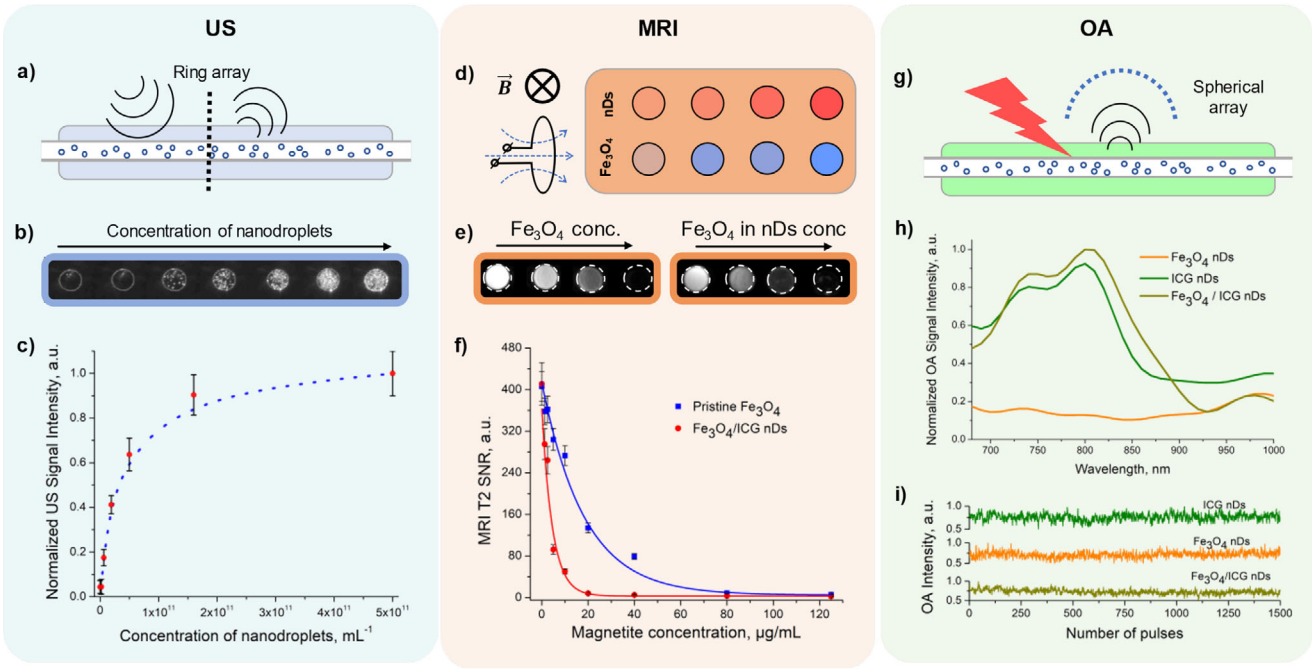

Figure 2. a) Schematic representation of US phantom measurements. b) US signal for different concentrations of nanodroplets in the cross section of the cylindrical phantom. c) Mean pixel intensity in the US images as a function of the nanodroplet concentration. d) Schematic representation of MRI phantom measurements. e) T2-weighted images of Fe_3O_4 nanoparticles and Fe_3O_4-containing nanodroplets for different magnetite concentrations. f) Signal-to-noise ratio (SNR) in T2 mode as a function of magnetite concentration. g) Schematic representation of OA measurements; h) OA spectra of nanodroplets with different compositions; i) Photostability of the nanodroplets at 800 nm. The signal intensity as a function of the number of pulses is shown.

neovasculature of some tumor types contains endothelial pores of up to 800 nm.[57] Therefore, these relatively large nanodroplets may accumulate in the tumor region through the enhanced permeability and retention (EPR) effect.[58]

To evaluate the loading efficiency for Fe_3O_4 and ICG, we measured the optical spectra of the supernatant liquids after each washing cycle. The spectra were compared to the calibration curves of each additive to determine the amount of nanoparticles and dye not adsorbed to the nanodroplets. The difference between the initial and final concentrations was considered to calculate the loading efficiency of additives. The iron content in the three layers was 0.54 ± 0.08 mg/mL which is 5.5 times higher as compared with the results of Xu et al.[59] (loading of oleic acid–capped magnetite into a PLGA-stabilized PFP core, 97 ± 3 µg mL^{-1}). Also, Niu et al.[60] loaded oleylamine-capped magnetite into the PFP core and found an iron element content of 6.7% w/w and tens of nanoparticles inside. Besides providing higher deposition efficiencies, the LbL approach allows avoiding additional functionalization of nanoparticles with hydrophobic capping agents and the use of as-prepared citrate-capped magnetite, which is inexpensive and easy to obtain. The measured ICG loading was 0.30 ± 0.08 mg of dye per mL of emulsion, yielding $3{\cdot}10^{-12}$ mg (3.9 µmol) per droplet. Previously, Hannah et al.[55] loaded ICG into the PFP core through tetrabutylammonium iodide–mediated phase transfer from chloroform to PFC, with a yield a higher loading efficiency of $5.8{\cdot}10^{-10}$ mg per droplet. Note, however, that the deposited amount of ICG is sufficient to provide strong OA contrast as shown later on.

2.2. Phantom Studies

US visualization of PFP nanodroplets was done with a ring-array transducer as described in the methods section. **Figure 2**a–c show a schematic representation of the measured phantom along with the dependence of the US signal on nanodroplet concentration. Unlike the case of gas-filled microbubbles, where the US signal is caused by bubble oscillations, the US signal for PFP nanodroplets is a consequence of consecutive evaporation and recondensation of the inner liquid PFP or the subsequent bubble burst. The low acoustic pressure at the region of interest (ROI) for the element-by-element excitation approach used for US imaging ensures that no inertial cavitation is produced for PFP droplets. The appearance of separate bright dots at lower concentrations (starting from $6.2{\cdot}10^{9}$ mL^{-1}) indicates that the applied negative pressure was sufficient to promote evaporation of the liquid core only for a small portion of nanodroplets in the cross–section. Previously, Qamar et al. concluded theoretically that the oscillation behavior may not start for a given PFC until droplets are below the threshold diameter.[61] With linearly increasing concentration, the US signal tended to exponentially increase. Note, however, that it saturates at higher concentrations. At the highest bubble concentration ($5{\cdot}10^{11}$ mL^{-1}), US signal increased by 23-fold with respect to the signal provided by pure water.

We also investigated the dependence of the MRI signal on the magnetite nanoparticle concentration. Droplet- and pure magnetite-loaded agar phantoms were placed in the phantom holder and positioned inside the MRI scanner as schematically depicted in Figure 2d. Figure 2e shows the T2-weighted MRI

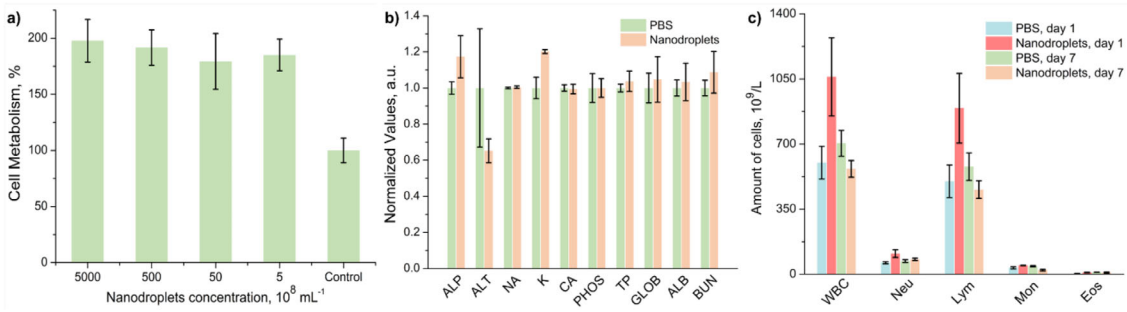

Figure 3. a) Results of alamarBlue cell viability assay of murine macrophages incubated with various concentrations of nanodroplets. Control –cells not exposed to droplets. b) Blood biochemistry of the PBS-injected mice (green) versus nanodroplets-injected mice (orange) taken 7 days post-injection. ALP - alkaline phosphatase, ALT - alanine transaminase, NA – sodium, K – potassium, CA – calcium, PHOS – phosphates, TP – total protein, GLOB – globulin, ALB – albumin, BUN – blood urea nitrogen c) Hematology of PBS-injected mice versus nanodroplets-injected mice at day 1 and 7 post-injection. WBC – white blood cells in total, Neu – neutrophils, Lym – lymphocytes, Mon – monocytes, Eos – eosinophils.

images of magnetite nanoparticles and magnetite-loaded nanodroplets. The magnetic resonance signal-to-noise ratio for samples containing a suspension of magnetite-loaded nanodroplets and magnetite colloids of the same concentration are displayed in Figure 2f.

MRI contrast agents are generally based on the T1-positive contrast of paramagnetic species and the T2-negative contrast of superparamagnetic particles.[62] The magnetite nanoparticles provided positive contrast in T1 mode and negative contrast in T2 mode, as also observed in prior work by our group.[48] Small-sized magnetite nanoparticles are capable of providing T1 contrast owing to the larger number of Fe^{3+} ions on the surface, suppressing T2 relaxation by their small magnetic moment.[63] Interestingly, magnetite-loaded nanodroplets showed a reversed tendency in the T1 mode (Figure S1, Supporting Information), thus giving a strong negative signal. This difference could be explained by the aggregation of nanoparticles in the polymeric shell. Previously, the dependence of the T1 signal on the size of iron oxide nanoparticles has been demonstrated by several groups.[64] Positive T1 contrast is typically produced for ultrasmall iron oxide nanoparticles. However, even a slight aggregation leads to a drastic loss of this effect. This indeed can be expected from the loading of nanoparticles in the polymeric shell, where they are forced to interact with each other in a way that some nanoparticles inevitably aggregate due to poor solvation.

In the T2 mode, as expected, the signal decreased drastically with increasing magnetite concentration. When loaded into the nanodroplet shell, the agents also showed negative T2 contrast, although the signal-to-noise ratio (SNR) decreased faster than for agar-dispersed nanoparticles (Figure 2f). Previously, Ni et al. proposed that the surface modification of magnetic nanoparticles impacts intrinsic surface spin disordering, increases inhomogeneity in the local magnetic field, or induces much stronger magnetization, leading to an enhanced T2 contrast.[65] We speculate that in this case, polyelectrolyte layers may have similar effects.

The OA spectra of the nanodroplets were measured in the wavelength range 690–1100 nm with a 10-nm step (Figure 2g–i). Note that the optical absorption spectra cannot be reliably measured due to the strong light scattering caused by the droplets. For all samples, the band near 1000 nm was attributed to absorption by water molecules and should not be considered a peak of interest. As expected, magnetite-only nanodroplets (Fe_3O_4 nDs) did not show any distinct peaks. Indeed, the optical absorption of magnetite nanoparticles is known to slightly decay toward longer wavelengths. The OA spectra of ICG nDs and Fe_3O_4/ICG nDs were approximately the same as that of free ICG with a slight red shift. Much like for other organic dyes, the rapid photobleaching (signal loss under continuous irradiation) of ICG is a major limitation for bioimaging.[66] Previously, it was shown by numerous groups that the presence of a polymer around the dye minimizes oxygen access, thus preventing the dye from undergoing chemical reactions that could lead to a loss in fluorescence intensity over time.[67,68] In this work, ICG is also entrapped between polymeric layers that act as a physical barrier between the dye molecules and the surrounding environment. To prove this, we examined the photostability of all samples at 800 nm (ICG absorption peak; Figure 2i) and at 700 nm (Figure S2, Supporting Information). No significant signal degradation was observed for any of the samples at either wavelength, even after exposure to 1500 laser pulses. Note that changes in the OA signal associated with explosive cavitation leading to the destruction of the droplets and PFP release were not observed. Note also that during in vivo imaging tissues were exposed to ≈700 pulses, i.e., less than half the pulses used in the photostability experiments.

2.3. Biocompatibility and Biosafety Studies

The biocompatibility and biosafety of the nanodroplets were assessed with in vitro and in vivo tests. First, the influence of the presence of nanodroplets on the viability of a murine macrophage culture was tested with an alamarBlue assay performed for 3 h on cell populations exposed to different concentrations of nanodroplets. This is particularly relevant since liver and spleen accumulation suggests that macrophages are the primary path of nanodroplet excretion and shell disassembling. The cellular uptake of nanodroplets was verified with optical microscopy images (Figure S4, Supporting Information). An increase in macrophage metabolism in the presence of nanodroplets was observed in comparison with PBS-fed cells. This could be explained by the increased activity of the cells due to the active digesting of the added substance and corroborates good cell viability (**Figure 3**a). Considering the higher signals

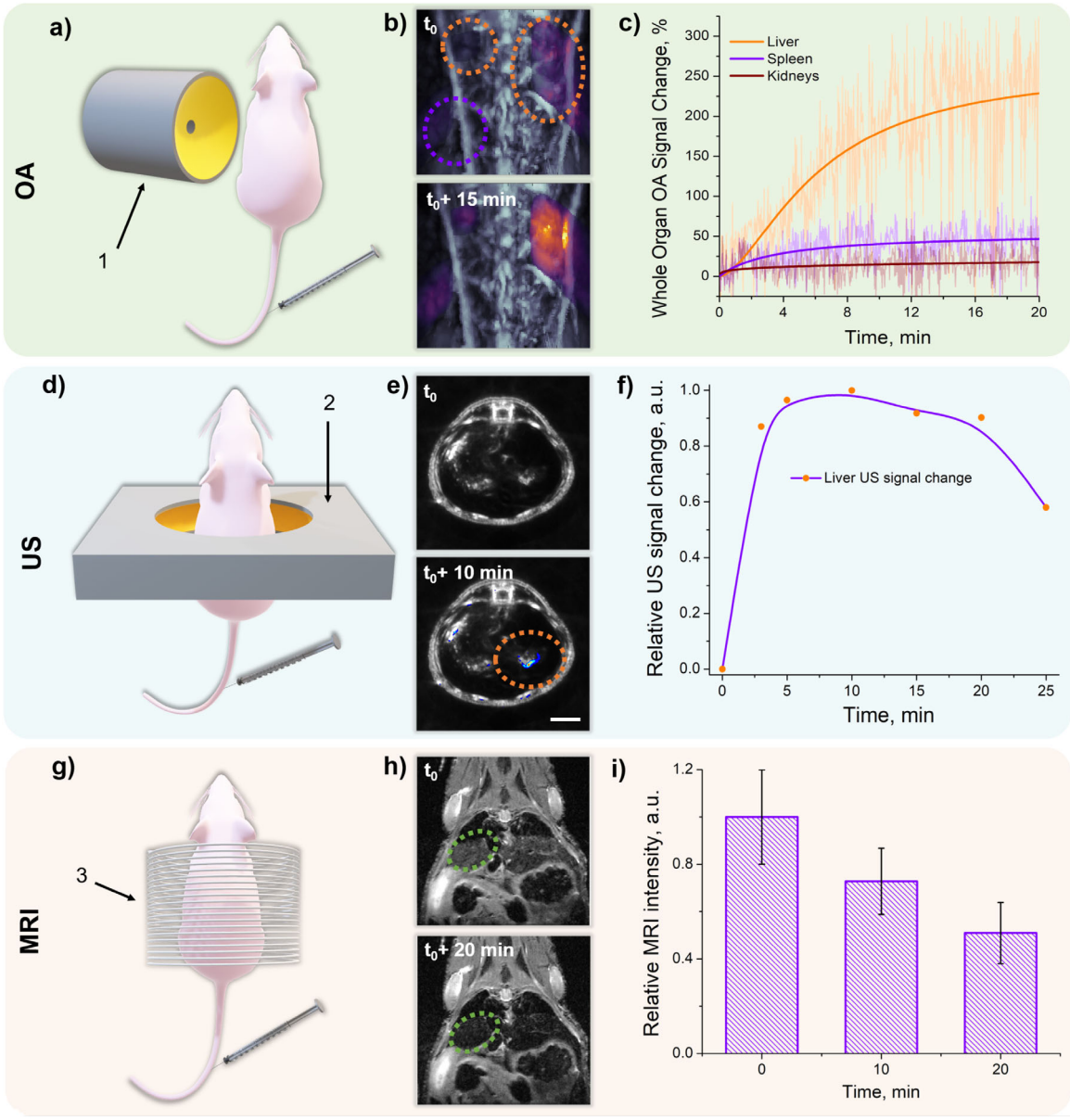

Figure 4. Upper panel: Single-sweep volumetric optoacoustic tomography (sSVOT) imaging of the kinetics of Fe_3O_4/ICG nDs in the mouse body. a) Schematic representation of the optoacoustic (OA) setup, 1 – spherical array transducer. b) Maximum intensity projections (MIPs) along the coronal view of the liver region of the mouse. Orange circles highlight the liver, and purple circle highlights the spleen. c) Biodistribution curves for the liver, spleen, and kidneys. Middle panel: ultrasound (US) imaging. d) Schematic representation of the US imaging setup; 2 – ring array transducer. e) Cross-sectional view of the liver region of the mouse before and 10 min after contrast agent administration. The orange circle highlights the nanodroplet accumulation point in the liver. f) Accumulation curve for the nanodroplets in the liver. Lower panel: MRI. g) Schematic representation of the MRI setup; 3 – MRI coil. h) MRI images of the mouse before and 20 min after contrast agent injection. Green circles show the region of interest (ROI) where the signal was measured. i) Evolution of the T2 signal within the selected ROI.

observed for cells exposed to nanodroplets and the insignificant difference in signal for different nanodroplet concentrations, we can conclude that no significant toxic effects are produced by the droplets.

The in vivo biosafety was also assessed with experiments performed in mice. No differences in behavior were observed between mice injected with nanodroplets and with PBS (controls). The weights of the mice were also not significantly affected (Figure S5, Supporting Information). On the other hand, biochemical and hematological parameters were also similar in the two groups of mice (Figure 3b,c).

2.4. In vivo Imaging

Following the phantom experiments demonstrating that sufficient contrast is provided in all modalities, in vivo experiments were performed. For this, 100 µL of a stock solution of Fe_3O_4/ICG

nDs (droplet concentration, $5{\cdot}10^{11}$ mL^{-1}; Fe_3O_4 concentration, 0.54 mg mL^{-1}; ICG concentration, 0.3 mg mL^{-1}) was injected through the mouse tail vein as described in the methods section. The clearance mechanism was determined by analyzing the OA signals for the spleen, liver, and kidneys collected for 20 min after injection. Figure 3a shows a schematic representation of the sSVOT imaging system used for collecting these data. Figures 4b,c show that the nanodroplets accumulated mostly in the liver, with a small amount found in the spleen. As expected, no large signal change was observed in the kidneys. This is expected considering that the cut-off diameter of kidney glomerular filtration is ≈5–10 nm, not permeable to ≈500-nm PFP droplets.[69]

The trimodal contrast performance was further tested with US and MRI images of the same murine region. Specifically, the particles at the stock concentration were injected and tracked in the mouse liver region with an US ring array transducer (**Figure 4**d). After the signal acquisition, the first (pre-injection) frame was subtracted from consecutive frames to reveal differential contrast (Figure 4e, colored part). Increased signal in the liver was observed for 25 min, with a peak around 10 min post–injection and a subsequent slow decay (Figure 4f). This could be assigned either to a partial burst of the microdroplets or to shell destruction followed by PFP release.

The MRI images were analyzed with ImageJ software. Figure 4g shows a schematic representation of the coil used for MRI data collection. The ROI assigned to the liver (green circle in Figure 3 h) was segmented on each frame, and the mean intensity was calculated. As expected, the signal for the liver region decreased by ≈20% every 10 min (Figure 4i), which indicated the accumulation of nanodroplets in the liver for the acquisition window of 20 min post–injection.

Overall, the collection of signals in the liver region, proven by OA imaging, US imaging, and MRI, indicates the long blood circulation of PFP droplets before they are uptaken by the reticuloendothelial system. From this standpoint, PFP nanodroplets represent a potential suitable replacement for existing commercial agents based on gas-filled microbubbles whose circulation half-life in blood does not exceed or is even less than several minutes.[70]

3. Conclusions

A new type of trimodal US-MRI-OA contrast agent based on a PFP liquid core and an absorbing multilayered shell consisting of biocompatible polyelectrolytes (PArg, PSS) alternating with ICG and magnetite nanoparticles was proposed. Contrary to the conventional gas core microbubbles used as US contrast agents, the liquid core ensures a more predictable behavior of the particles during synthesis and increased the storage stability of the agents. PFP nanodroplets with an average size of 500 nm were successfully prepared. 0.23 mg mL^{-1} of magnetite and 0.3 mg mL^{-1} of ICG were deposited onto their shells by the LbL technique. The proof-of-concept study in this work showed that US, MRI and OA contrast can be combined "all in one". The US signal can be amplified either by PFP core vaporization–recondensation cycles or by the large acoustic impedance difference between the formed gas-filled bubble and surrounding tissues. MRI contrast was straightforwardly provided by superparamagnetic magnetite nanoparticles in the shell, whereas ICG incorporation secured an enhanced OA signal. The increase in contrast in MRI, US and OA imaging was first clearly shown in phantom studies. Presented nanodroplets demonstrate good cell biocompatibility in the study on murine macrophage cell line and showed good biosafety level. Subsequently, in vivo contrast was also demonstrated in experiments with mice. These studies further enabled assessing the dynamic bio-distribution of the nanodroplets, which revealed that their blood circulation half-life was substantially prolonged with respect to commercially available agents.

To sum up, the trimodal nanodroplets proposed and developed in this work are promising particles for biomedical applications with hybrid US-MRI-OA systems expected to emerge in the following years after the feasibility demonstration of this multimodal approach. Further developments will be focused on synthetic route improvement and on the development of targeted molecular imaging applications.

4. Experimental Section

Materials: Bovine serum albumin (BSA), iron (III) chloride hexahydrate ($FeCl_3{\cdot}6H_2O$), iron (II) chloride tetrahydrate ($FeCl_2{\cdot}4H_2O$), sodium hydroxide (NaOH), citric acid ($C_6H_8O_7$), tannic acid (TA; $C_{76}H_{52}O_{46}$), poly-L-arginine hydrochloride (PArg; M_w > 70000), polystyrene sulfonate (PSS; M_w > 70000), agar, and low-gelling-point agar were all purchased from Sigma–Aldrich and were used without additional purification. *N*-perfluoropentane (99%; C_5F_{12}, PFP) was obtained from FluoroMed, L.P. Indocyanine green (ICG) was purchased from MP Biomedicals, LLC (France). Cell culture medium (DMEM), alamarBlue cell assay kit, fetal bovine serum (FBS) and 96-well plates were purchased from Thermo Fisher Scientific Inc. J774A.1 murine macrophages were obtained from CLS Cell Lines Service GmbH. Double-deionized water (specific resistivity18.2 MΩ cm; Milli-Q Integral 3 water purification system, Millipore, MA) was used to make all solutions.

Magnetite Nanoparticles: Magnetite (Fe_3O_4) nanoparticles were prepared by coprecipitation of Fe^{2+} and Fe^{3+} salts in an alkaline medium.[71] A TetraQuant CR-1 automated reactor (TetraQuant LLC, Russia) was used for the synthesis of nanoparticles.[72] This reactor ensures accurate control over the feed of components into the reaction beaker and maintains an inert atmosphere during synthesis. The resulting nanoparticles were stabilized with 0.1 M citric acid and were dialyzed in deionized water at room temperature for 4 days. The concentration of the resulting colloid was measured by colorimetric titration to be 1.38 ± 0.01 mg mL^{-1}. For colorimetric titration, sulfuric acid was added to a Fe_3O_4 aliquot to completely dissolve colloids. 24 h later, the concentration of Fe^{3+} (as a thiocyanate complex) was estimated by measuring the absorption of the solution with a Tecan Infinite 200 PRO multimode plate reader. For calculating the magnetite amount, the absorption level was compared with that of the standard Fe solution. The average size and ζ-potential of the nanoparticles were measured with a Malvern Zetasizer Nano ZS analyzer (Malvern Panalytical, Malvern, UK). The measured values were 9 ± 2 nm and -30 ± 6 mV, respectively.

Submicron PFP Droplets: The synthesis methodology of PFP-nanodroplets (nDs) was adopted from Hannah et al.[55] Briefly, 2.7 mL of a BSA solution in deionized water (2 mg mL^{-1}) was placed in a glass vial and kept on ice for 5 min. A 0.3-mL portion of PFP was added and the solution was kept on ice to prevent evaporation of PFP (boiling point, 29 °C). The vial was then vigorously shaken on a Mini Vortexer running at maximum speed for 30 s to emulsify PFP into submillimeter droplets. Next, the sonotrode tip was placed at the lower part of the vial close to the water–PFP interface and the solution was sonicated at 100 W for 3 min (frequency, 40 kHz). After sonication, the emulsion turned milky white because of the formation of submicron nanodroplets. The Laplace pressure increases the boiling point of droplets to 70 °C

or higher, depending on size[55] (see theoretic prediction in Supporting Information). For further use, the droplets were washed three times by centrifugation at 1100 rcf for 1 min.

LbL Assembly on PFP Droplets: Freshly prepared submicron-sized BSA–PFP nanodroplets were washed free of unbound BSA molecules. A layered shell was made by successive absorption of 2 mL of TA (2 mg mL^{-1}), polyelectrolytes (PArg, 0.15 mg mL^{-1}; PSS, 1 mg mL^{-1}), magnetite nanoparticles (0.2 mg mL^{-1}), and ICG (1 mg mL^{-1}) solutions. After the addition of each solution, the sample was vortexed on a Vortex-Genie 2 (Scientific Industries, New York, USA) at power 5 for 15 min. The sample was washed free of unbound compounds by centrifugation at 1100 rcf for 2 min, after which it was washed three times with deionized water.

Four types of samples were prepared. For the control nanodroplet sample (blank nDs, no functional additives), the following sequence was applied to the initial BSA core: $TA/(PArg/PSS)_6$. For the magnetite-containing sample (Fe_3O_4 nDs), instead of PSS layers, a hydrosol of citrate-capped magnetite nanoparticles was used to achieve the following sequence of layers: $TA/(PArg/Fe_3O_4)_3/(PArg/PSS)_3$. For ICG incorporation (ICG nDs), droplets with three bilayers were coated with yet another layer of PArg and then with a layer of ICG. These steps were repeated twice. The final sequence of layers was as follows: $TA/(PArg/PSS)_3/(PArg/ICG)_2(PArg/PSS)$. For simultaneously incorporating magnetite nanoparticles and ICG in the shell (Fe_3O_4/ICG nDs), droplets with three layers of magnetite nanoparticles were coated with PArg and ICG, so that the resulting sequence of layers was as follows: $TA/(PArg/Fe_3O_4)_3(PArg/ICG)_2(PArg/PSS)$.

Size and ζ-Potential Measurements: Dynamic light scattering (DLS) and ζ-potential measurements were made on the Zetasizer Nano ZS analyzer. For ζ-potential measurements, all samples were diluted ≈20 times in deionized water and placed in a folded capillary cell (DTS1070, Malvern). For size distribution measurements, all samples were diluted ≈40 times in deionized water and placed in a plastic cuvette. Results were processed with Zetasizer software 8.00. Each measurement was made at 25°C and repeated three times.

Scanning Electron Microscopy: All samples were deposited on a dried *p*-doped silicon chip (Electron Microscopy Sciences, USA) precleaned with ethanol in an ultrasonic bath. The samples were then mounted on a scanning electron microscopy (SEM) stub by using carbon duct tape. SEM microphotographs were obtained on a Hitachi SU5000 microscope (Hitachi High-Tech Corp., Japan) at an accelerating voltage of 3.0 kV in both secondary electron and backscattered electron modes.

Ultrasound Imaging: Phantoms containing nanodroplets were imaged with US. These were prepared as follows. 500 mg of agar was dissolved in 500 mL of deionized water and heated to 100 °C under stirring. The resultant hot solution was poured into a cylindrical plastic mold with a 20 mm diameter, and a cylindrical wooden rod with a diameter of 4 mm was placed at the center to make a hollow channel. Then, the phantom was left to solidify at 4 °C, and the stick was removed slowly in order not to damage the channel. For imaging, the phantoms were vertically immersed in water with the open end of the channel positioned above the water surface. A suspension of nanodroplets (300 µL) was injected in the channel immediately before measurement to prevent the diffusion of droplets through agarose pores and sedimentation during the experiment. A series of threefold dilutions starting from concentration $5{\cdot}10^{11}$ cm^{-3} were prepared to track the dependence of the signal on nanodroplet concentration.

The phantoms were imaged as described elsewhere.[73,74] Briefly, short pulses consisting of one cycle of a bipolar signal (38 Vpp) with a duration of 0.16 µs were subsequently sent to each element of a full-ring array of cylindrically focused elements. The peak central frequency and the transmission/reception bandwidth of the array elements were 5 MHz and 60% at −6 dB, respectively. Pulse-echo US imaging was performed with the synthetic transmit aperture technique based on single-element transmission and simultaneous reception with all elements. The pulse transmission events were repeated sequentially for all 512 elements (360° full coverage). Then, the images from each transmission event were reconstructed with the delay-and-sum algorithm,[74] and eventually coherently compounded to form the final image.

Optoacoustic Spectroscopy and Photostability Characterization: The setup used for OA imaging was described previously.[75] Briefly, a low-density polyethylene (LDPE) tubing (inner diameter, 1.25 mm) was filled with a microbubble suspension and placed at the center of the field of view (FOV) of a spherical array transducer. The peak central frequency and the reception bandwidth of the array elements were 4 MHz and >80% at −6 dB, respectively.[76] The tube was embedded inside a 1% (w/v) agar matrix filling the spherical volume enclosed by the array for better coupling of the generated OA signals to the array elements. The laser excitation source was swept over the wavelength range 700–1100 nm with a 10-nm interval. A total of 25 frames were averaged at each wavelength to obtain the OA spectrum of each sample.

For photostability measurements, an LDPE tubing was filled with a microbubble suspension in the same way as for OA spectroscopy measurements. The samples were illuminated with 2400 pulses at wavelengths of 700 and 800 nm separately. 800 nm was chosen as it corresponds to the ICG absorption peak, and 700 nm was chosen because the magnetite extinction coefficient at this wavelength was higher than that of ICG. Note that the total number of pulses irradiated on the nanoparticles was well above the number of pulses irradiated on each volumetric frame during in vivo scanning.

The same setup was used to determine the dependence of the OA signal on the nanodroplet concentration. The initial nanodroplet suspension was diluted with deionized water to make solutions with magnetite concentrations of 0.005, 0.013, 0.032, 0.08, 0.2, and 0.5 mg mL^{-1} and with ICG concentrations of 0.78, 1.92, 4.8, 12, 30, and 75 µM.

Magnetic Resonance Imaging: MRI was performed on a 9.4 T small-animal scanner (Bruker, Ettlingen, Germany) with a bore of 30 cm and a gradient insert with a gradient strength of 660 mT m^{-1}. A circularly polarized volume coil was used for radio-frequency excitation, and a cryogenically cooled 2 × 2 array surface coil was used for signal reception. T1-weighted images were collected with a FLASH sequence with TR/TE = 200/4 ms. T2-weighted images were acquired with a RARE sequence with a rare factor of 4, TR/TE = 3000/45 ms. T1 maps were acquired with a saturation recovery sequence with TE = 8 ms and eight TR values ranging from 25 to 3000 ms, which were fitted exponentially to retrieve the T1 values of the samples. T2 maps were acquired with a spin echo sequence with TR = 2000 ms and 25 TE values ranging from 7 to 175 ms.

Phantoms containing nanodroplets or magnetite nanoparticles were imaged with MRI. These were prepared as follows. First, a solution of 1% low-gelling-point agar was prepared. The initial suspension of nanodroplets or nanoparticles was diluted with a warm agar solution to reach magnetite concentrations of 0, 1.25, 2.5, 5, 10, 20, 40, 80, and 125 µg mL^{-1}. A 40-µL aliquot of each as-prepared solution was placed in one well of the phantom holder and was left to quickly solidify on the cold plate to avoid precipitation before solidification.

Cell Metabolism Test: The biocompatibility of nanodroplets was assessed with an alamarBlue assay carried out on a murine macrophage cell culture. First, cells were cultivated in DMEM supplemented with 10% FBS in a humidified incubator at 37 °C in 5% CO_2. After that, a 96-well plate was seeded with 8×10^3 cells per well, and filled with 200 µL of cell medium without an indicator. 20 µL of the emulsion of different concentrations of nanodroplets (from 5×10^8 until 5×10^{11} mL^{-1}) were added to each row of the well plate (10 wells per row), leaving one row as the control corresponding to cells fed with PBS. After 48 h of incubation, cells were washed with PBS and 20 µL of alamarBlue stock solution was added according to the standard protocol to each well. Cells were then additionally left for incubation for 3 h. After that, 100 µL of the cell-processed medium was transferred to a fresh 96-well plate to form a reading replica without an influence of cells and residual nanodroplets inside them. The reading replica was then loaded into the well-plate reader (Tecan Infinite M200) and the fluorescence of the medium was measured at 540 nm excitation and 590 nm emission wavelengths.

In vivo Biosafety Test: The biosafety of the droplets was assessed in female Swiss mice (n = 6, 7 weeks old). These were split into control (n = 3) and experimental (n = 3) groups injected i.v. with a single dose of 100 µl of saline and the nanodroplet emulsion

(5×10^{11} droplets/mL^{-1}), respectively. Animals were randomly assigned to the two groups. Mice were scored and weighted at days 1, 4, 6, and 7 following i.v. administration and subsequently sacrificed. Hematological analysis of blood samples was performed by using a Mindray BC5000-Vet analyzer at days 1 and 7 post-injection. Clinical biochemistry was performed in a VetScan VS2 analyzer (Zoetis) by using a Comprehensive Diagnostic Profile at the final time point with the collected serum samples. The biosafety study was done in accordance with Spanish and European regulations and approved by the Xunta de Galicia.

Animal Imaging Experiments: All in vivo animal imaging experiments were conducted in full accordance with the Swiss Federal Act on Animal Protection and with the approval of the Cantonal Veterinary Office of Zurich. In all experiments, the animals were euthanized while still under anesthesia. All animals were housed in ventilated cages inside a temperature-controlled room under a 12 h dark/light cycle. The temperature was 21 ± 1 °C, with a relative humidity of 55 ± 10%. Pelleted food and water were provided ad-libitum.

Kinetics of Nanodroplets in vivo: The nanodroplet kinetics and biodistribution in mice were investigated with a state-of-the-art full-body OA imaging system. For this, a female athymic nude Foxn1nu mouse was imaged following injection of a 100-µL bolus of a suspension of nanodroplets (concentration, $\approx 5 \cdot 10^{11}$ cm^{-3}). Imaging was performed with a recently-reported single-sweep volumetric optoacoustic tomography (sSVOT) system.[75,77] A custom-made animal holder was used to place a mouse inside a water tank in a fixed stationary position with its fore and hind paws attached. Throughout the experiments, water was stabilized at 36 °C with a feedback-controlled heating unit. During data acquisition, the mice remained inactive under isoflurane anesthesia (Abbott, Cham, Switzerland, volume ratio for induction, 5%; volume ratio during experiments, 1.5%) in an oxygen/air mixture (100/400 mL/min). Vet ointment (Bepanthen, Bayer AG, Leverkusen, Germany) was applied to the eyes of the mouse to prevent dehydration during scanning and to protect them from laser light. The mouse was positioned inside the imaging setup, and 100 µL of the Fe_3O_4/ICG nDs emulsion was injected intravenously via a tail catheter. The laser delivered <10-ns pulses at 800 nm with an energy of up to ≈125 mJ per pulse at a frequency of 10 Hz. The mouse was scanned on the back from head to tail at a scan speed of 80 mm s^{-1}. The generated OA responses were collected at multiple locations around the imaged volume with a custom-made spherical array of 512 ultrasound sensors, each having an area of ≈7 mm^2, a central detection frequency of 7 MHz, and a full width at half maximum (FWHM) bandwidth of ≈85%. The OA signals were simultaneously digitized at 40 MHz with a custom-made parallel data acquisition unit (Falkenstein Mikrosysteme GmBH, Taufkirchen, Germany) triggered by the Q-switch output of the laser and stored in a computer for further processing. Data acquisition was controlled by using a computer with MATLAB.

In vivo Ultrasound Imaging: The same system described in the US imaging section was used to image a mouse in vivo. A custom-made animal holder was used to place the mouse inside a water tank in a fixed stationary position with its fore and hind paws attached. Throughout the experiments, water was stabilized at 36 °C with a feedback-controlled heating unit. During data acquisition, the mouse remained inactive under isoflurane anesthesia (Abbott, Cham, Switzerland, volume ratio for induction, 5%; volume ratio during experiments, 1.5%) in an oxygen/air mixture (100/400 mL/min). Following induction of anesthesia, the mouse was mounted inside the transducer and imaging of the liver region was performed. A bolus of 100 µL of Fe_3O_4/ICG nDs was injected via the tail vein, and signals were acquired at 5-min intervals for 25 min.

In vivo MRI Imaging: The mouse was mounted inside a 1 H receive-only 8×1 mouse body surface array coil and inserted into the bore of the MRI scanner. During data acquisition, the mouse remained inactive under isoflurane anesthesia (Abbott, Cham, Switzerland, volume ratio for induction, 4%; volume ratio during experiments, 1.5%) in an oxygen/air mixture (100/400 mL/min). After the region of interest was localized, the mouse was injected with 100 µL of Fe_3O_4/ICG nDs via the tail vein and was monitored afterwards in the T2 RARE-imaging mode with a repetition time of 2 s.

Supporting Information

Supporting Information is available from the Wiley Online Library or from the author.

Acknowledgements

X.L.D.B. acknowledges support from the Helmut Horten Stiftung (project Deep Skin). D.R. acknowledges support from the European Research Council (grant no. ERC-2015-CoG-682379) and the National Institutes of Health (grant no. UF1-NS107680). The authors thank Dr. Sergei German and TetraQuant LLC for the synthesis and characterization of magnetite nanoparticles. This work was supported by the Russian Foundation for Basic Research (RFBR grant no. 19-53-80047 BRICS_t). A.A.S. and Y.M acknowledge support from the National Natural Science Foundation of China (grant no. 51961145108). The authors gratefully acknowledge ScopeM for their support and assistance in this work.

Conflict of Interest

The authors declare no conflict of interest.

Author Contributions

E.A.M. and D.N. contributed equally to this work. The manuscript was written through the contributions of all authors. All authors have given approval to the final version of the manuscript.

Data Availability Statement

The data that support the findings of this study are available from the corresponding author upon reasonable request.

Keywords

indocyanine green, magnetic resonance imaging, magnetite nanoparticles, multilayer polymer shell, optoacoustic imaging, perfluoropentane nanodroplets, photoacoustic imaging, polyelectrolytes, ultrasound

Received: February 13, 2023
Revised: May 18, 2023
Published online:

[1] A. L. Klibanov, J. A. Hossack, *Invest Radiol* **2015**, *50*, 657.
[2] H. Lutz, E. Buscarini, W. H. Organization, 2011, Published by the World Health Organization in coll.
[3] S. Kaul, *Circulation* **2008**, *118*, 291.
[4] C. Demené, J. Robin, A. Dizeux, B. Heiles, M. Pernot, M. Tanter, F. Perren, *Nat. Biomed. Eng.* **2021**, *5*, 219.
[5] A. Karlas, N. A. Fasoula, K. Paul-Yuan, J. Reber, M. Kallmayer, D. Bozhko, M. Seeger, H. H. Eckstein, M. Wildgruber, V. Ntziachristos, *J. Photoacoust.* **2019**, *14*, 19.
[6] J. Weber, P. C. Beard, S. E. Bohndiek, *Nat. Methods* **2016**, *13*, 639.
[7] X. L. Deán-Ben, S. Gottschalk, B. Mc Larney, S. Shoham, D. Razansky, *Chem. Soc. Rev.* **2017**, *46*, 2158.
[8] M. Omar, J. Aguirre, V. Ntziachristos, *Nat. Biomed. Eng.* **2019**, *3*, 354.
[9] L. Li, L. V. Wang, *BME Front.* **2021**, *2021*, 9823268.
[10] F. Knieling, C. Neufert, A. Hartmann, J. Claussen, A. Urich, C. Egger, M. Vetter, S. Fischer, L. Pfeifer, A. Hagel, C. Kielisch, R. S. Görtz, D. Wildner, M. Engel, J. Röther, W. Uter, J. Siebler, R. Atreya, W. Rascher, D. Strobel, M. F. Neurath, M. J. Waldner, *N. Engl. J. Med.* **2017**, *376*, 1292.

[11] A. P. Regensburger, L. M. Fonteyne, J. Jüngert, A. L. Wagner, T. Gerhalter, A. M. Nagel, R. Heiss, F. Flenkenthaler, M. Qurashi, M. F. Neurath, N. Klymiuk, E. Kemter, T. Fröhlich, M. Uder, J. Woelfle, W. Rascher, R. Trollmann, E. Wolf, M. J. Waldner, F. Knieling, *Nat. Med.* **2019**, *25*, 1905.
[12] A. B. E. Attia, G. Balasundaram, M. Moothanchery, U. S. Dinish, R. Bi, V. Ntziachristos, M. Olivo, *J. Photoacoust.* **2019**, *16*, 100144.
[13] J. Kim, D. Lee, U. Jung, C. Kim, *Ultrasonography* **2015**, *34*, 88.
[14] X. L. Deán-Ben, E. Merčep, D. Razansky, *Appl. Phys. Lett.* **2017**, *110*, 203703.
[15] M. Oeri, W. Bost, N. Sénégond, S. Tretbar, M. Fournelle, *Ultrasound Med Biol* **2017**, *43*, 2200.
[16] P. J. van den Berg, K. Daoudi, H. J. Bernelot Moens, W. Steenbergen, *J. Photoacoust.* **2017**, *8*, 8.
[17] W. Ren, X. L. Deán-Ben, M. Augath, D. Razansky, *J Biophotonics* **2021**, *14*, https://doi.org/10.1002/jbio.202000293.
[18] Z. Chen, I. Gezginer, M.-A. Augath, W. Ren, Y.-H. Liu, R. Ni, X. L. Deán-Ben, D. Razansky, *Light Sci Appl* **2022**, *11*, 332.
[19] Z. Chen, I. Gezginer, M. Augath, Y. Liu, R. Ni, X. L. Deán-Ben, D. Razansky, *Adv. Sci.* **2022**, 2205191.
[20] B. B. Goldberg, J. Bin Liu, F. Forsberg, *Ultrasound Med Biol* **1994**, *20*, 319.
[21] D. Cosgrove, *Eur J Radiol* **2006**, *60*, 324.
[22] C. F. G. C. Geraldes, S. Laurent, *Contrast Media Mol. Imaging* **2009**, *4*, 1.
[23] J. Wahsner, E. M. Gale, A. Rodríguez-Rodríguez, P. Caravan, *Chem. Rev.* **2019**, *119*, 957.
[24] M. Laramie, M. Smith, F. Marmarchi, L. McNally, M. Henary, *Molecules* **2018**, *23*, 2766.
[25] R. E. Noskov, A. Machnev, I. I. Shishkin, M. V. Novoselova, A. V. Gayer, A. A. Ezhov, E. A. Shirshin, S. V. German, I. D. Rukhlenko, S. Fleming, B. N. Khlebtsov, D. A. Gorin, P. Ginzburg, *Adv. Mater.* **2021**, *33*, 2008484.
[26] J. Mujtaba, J. Liu, K. K. Dey, T. Li, R. Chakraborty, K. Xu, D. Makarov, R. A. Barmin, D. A. Gorin, V. P. Tolstoy, G. Huang, A. A. Solovev, Y. Mei, *Adv. Mater.* 2007465, **2021**, *33*.
[27] M. D. Pagel, *Nanomedicine* **2011**, *6*, 945.
[28] J. Rieffel, U. Chitgupi, J. F. Lovell, *Small* **2015**, *11*, 4445.
[29] J. C. Hsu, P. C. Naha, K. C. Lau, P. Chhour, R. Hastings, B. F. Moon, J. M. Stein, W. R. T. Witschey, E. S. McDonald, A. D. A. Maidment, D. P. Cormode, *Nanoscale* **2018**, *10*, 17236.
[30] A. Dauba, A. Delalande, H. A. S. Kamimura, A. Conti, B. Larrat, N. Tsapis, A. Novell, *Pharmaceutics* **2020**, *12*, 1125.
[31] D. Zhuang, H. Zhang, G. Hu, B. Guo, *J Nanobiotechnology* **2022**, *20*, 284.
[32] F. Kiessling, S. Fokong, J. Bzyl, W. Lederle, M. Palmowski, T. Lammers, *Adv. Drug Delivery Rev.* **2014**, *72*, 15.
[33] P. S. Sheeran, P. A. Dayton, *Scientifica (Cairo)* **2014**, *2014*, 579684.
[34] E. Strohm, M. Rui, I. Gorelikov, N. Matsuura, M. Kolios, *Biomed. Opt. Express* **2011**, *2*, 1432.
[35] E. Stride, T. Segers, G. Lajoinie, S. Cherkaoui, T. Bettinger, M. Versluis, M. Borden, *Ultrasound Med Biol* **2020**, *46*, 1326.
[36] A. S. Hannah, G. P. Luke, S. Y. Emelianov, *Theranostics* **2016**, *6*, 1866.
[37] H. Yoon, *Photonics* 405, **2021**, *8*.
[38] Y. Xu, W. Li, S. Chen, B. Huang, W. Pei, C. Niu, *Front Bioeng Biotechnol* **2020**, *8*, 599107.
[39] A. Schmid, L. R. Sutton, S. P. Armes, P. S. Bain, G. Manfrè, *Soft Matter* **2009**, *5*, 407.
[40] C.-Y. Lin, W. G. Pitt, *Biomed Res. Int.* **2013**, *2013*, 404361.
[41] Z. Huang, J. Xin, K. Li, *BMC Gastroenterol.* **2021**, *21*, 487.
[42] C. Niu, Y. Xu, S. An, M. Zhang, Y. Hu, L. Wang, Q. Peng, *Sci. Rep.* **2017**, *7*, 5490.
[43] L. Wang, S. Chen, Y. Zhu, M. Zhang, S. Tang, J. Li, W. Pei, B. Huang, C. Niu, *ACS Appl. Mater. Interfaces* **2018**, *10*, 42102.
[44] J. E. Lemaster, F. Chen, T. Kim, A. Hariri, J. V. Jokerst, *ACS Appl. Nano Mater* **2018**, *1*, 1321.
[45] G. Decher, J.-D. Hong, *Makromol. Chemie. Macromol. Symp.* **1991**, *46*, 321.
[46] A. P. R. Johnston, C. Cortez, A. S. Angelatos, F. Caruso, *Curr. Opin. Colloid Interface Sci.* **2006**, *11*, 203.
[47] H. Ai, *Adv. Drug Delivery Rev.* **2011**, *63*, 772.
[48] S. V. German, D. N. Bratashov, N. A. Navolokin, A. A. Kozlova, M. V. Lomova, M. V. Novoselova, E. A. Burilova, V. V. Zyev, B. N. Khlebtsov, A. B. Bucharskaya, G. S. Terentyuk, R. R. Amirov, G. N. Maslyakova, G. B. Sukhorukov, D. A. Gorin, *Phys. Chem. Chem. Phys.* **2016**, *18*, 32238.
[49] A. M. Yashchenok, D. N. Bratashov, D. A. Gorin, M. V. Lomova, A. M. Pavlov, A. V. Sapelkin, B. S. Shim, G. B. Khomutov, N. A. Kotov, G. B. Sukhorukov, H. Möhwald, A. G. Skirtach, *Adv. Funct. Mater.* **2010**, *20*, 3136.
[50] M. V. Novoselova, S. V. German, T. O. Abakumova, S. V. Perevoschikov, O. V. Sergeeva, M. V. Nesterchuk, O. I. Efimova, K. S. Petrov, V. S. Chernyshev, T. S. Zatsepin, D. A. Gorin, *Colloids Surf., B* **2021**, *200*, 111576.
[51] A. A. Antipov, D. Shchukin, Y. Fedutik, A. I. Petrov, G. B. Sukhorukov, H. Möhwald, *Colloids Surfaces A Physicochem. Eng. Asp.* **2003**, *224*, 175.
[52] M. Ahmed, B. Gustafsson, S. Aldi, P. Dusart, G. Egri, L. M. Butler, D. Bone, L. Dähne, U. Hedin, K. Caidahl, *Cell. Mol. Bioeng.* **2019**, *12*, 15.
[53] D. G. Shchukin, K. Köhler, H. Möhwald, G. B. Sukhorukov, *Angew. Chemie - Int Ed.* **2005**, *44*, 3310.
[54] M. Szczęch, K. Szczepanowicz, *Nanomaterials* **2020**, *10*, 496.
[55] A. Hannah, G. Luke, K. Wilson, K. Homan, S. Emelianov, *ACS Nano* **2014**, *8*, 250.
[56] E. Kaspchak, A. C. Goedert, L. Igarashi-Mafra, M. R. Mafra, *Int. J. Biol. Macromol.* **2019**, *136*, 486.
[57] S. K. Hobbs, W. L. Monsky, F. Yuan, W. G. Roberts, L. Griffith, V. P. Torchilin, R. K. Jain, *Proc Natl Acad Sci U S A* **1998**, *95*, 4607.
[58] A. K. Iyer, G. Khaled, J. Fang, H. Maeda, *Drug Discov Today* **2006**, *11*, 812.
[59] Y. Xu, C. Niu, S. An, S. Tang, P. Xiao, Q. Peng, L. Wang, *RSC Adv.* **2017**, *7*, 40791.
[60] D. Niu, X. Wang, Y. Li, Y. Zheng, F. Li, H. Chen, J. Gu, W. Zhao, J. Shi, *Adv. Mater.* **2013**, *25*, 2686.
[61] A. Qamar, Z. Z. Wong, J. B. Fowlkes, J. L. Bull, *Appl. Phys. Lett.* **2010**, *96*, 143702.
[62] Y.-D. Xiao, R. Paudel, J. Liu, C. Ma, Z.-S. Zhang, S.-K. Zhou, *Int J Mol Med* **2016**, *38*, 1319.
[63] J. Huang, L. Wang, X. Zhong, Y. Li, L. Yang, H. Mao, *J. Mater. Chem. B* **2014**, *2*, 5344.
[64] Z. Lu, J. Yan, M. Xu, L. Sun, J. Liu, Y. Zhang, L. Shi, X. Fei, Y. Cao, R. Pei, *ACS Appl. Nano Mater.* **2023**, *6*, 119.
[65] D. Ni, W. Bu, E. B. Ehlerding, W. Cai, J. Shi, *Chem. Soc. Rev.* **2017**, *46*, 7438.
[66] C. D. Geddes, H. Cao, J. R. Lakowicz, *Spectrochim. Acta Part A Mol. Biomol. Spectrosc.* **2003**, *59*, 2611.
[67] M. Kolitz-Domb, I. Grinberg, E. Corem-Salkmon, S. Margel, *J Nanobiotechnology* **2014**, *12*, 30.
[68] V. Saxena, M. Sadoqi, J. Shao, *J Photochem Photobiol B* **2004**, *74*, 29.
[69] P. Cheng, K. Pu, *Nat. Rev. Mater.* **2021**, *6*, 1095.
[70] M. Schneider, *Echocardiography* **2007**, *16*, 743.
[71] R. Massart, *IEEE Trans Magn* **1981**, *17*, 1247.

[72] S. V. German, O. A. Inozemtseva, A. V. Markin, K. Metvalli, G. B. Khomutov, D. A. Gorin, *Colloid J.* **2013**, *75*, 483.
[73] B. Lafci, E. Merčep, J. L. Herraiz, X. L. Deán-Ben, D. Razansky, *Neoplasia* **2020**, *22*, 770.
[74] B. Lafci, J. Robin, X. L. Dean-Ben, D. Razansky, *IEEE Trans Ultrason Ferroelectr Freq Control* **2022**, 2837.
[75] S. K. Kalva, A. Sánchez-Iglesias, X. L. Deán-Ben, L. M. Liz-Marzán, D. Razansky, *ACS Appl. Mater. Interfaces* **2022**, *14*, 172.
[76] X. L. Deán-Ben, D. Razansky, *Opt. Express* **2013**, *21*, 28062.
[77] S. K. Kalva, X. L. Dean-Ben, D. Razansky, *Photonics Res* **2021**, *9*, 899.